The 9th European Congress on Computational Methods in Applied Sciences and Engineering
ECCOMAS Congress 2024
3–7 June 2024, Lisboa, Portugal

NUMERICAL MODELLING OF MULTI-PLY POLYMERIC CORDS

LUCAS PIRES DA COSTA[1,*], MARCO MOSCATELLI[1], PAOLA CARACINO[2], GIORGIO NOVATI[1] AND CLAUDIA COMI[1]

[1] Department of Civil and Environmental Engineering, Politecnico di Milano
piazza Leonardo da Vinci 32, 20133 Milan – Italy, lucas.piresdacosta@polimi.it
[2] R&D Materials, Reinforcements Group, Pirelli Tyres SpA, 20126 Milan – Italy,
paola.caracino@pirelli.com

Key words: Polymeric cords, Tyres, Finite elements, Elasto-viscoplastic model

Summary. Textile reinforcements in the form of polymeric cords are currently employed in rubber composites used in tyres as a lighter alternative to metallic wires. The cords are typically composed of two or three twisted yarns, each one made of several hundreds of filaments. Their numerical modelling is challenging due to the different scales involved, the geometric nonlinear effects, and the filament material's constitutive nonlinearity. In the present work, we consider multi-ply rayon cords and we further develop a methodology that, using a viscoelastic-viscoplastic constitutive model, an analytical description of the filaments trajectory and the experimental measurement of the cord cross section, allows to define the inclination of the material directions at each point of an equivalent anisotropic cylinder to be used in numerical simulation. The numerical predictions are compared with experimental data on 3-ply rayon cords in uniaxial tests conducted at different strain rates and in three-point bending tests.

1 INTRODUCTION

The overall behaviour of cords is highly dependent on the trajectory of the constituent filaments, which can be reconstructed accurately only with complex experimental techniques, e.g. combining X-ray microtomography and image processing, as reported in [1] with reference to 2-ply and 3-ply nylon cords. In [2], we developed a model for the simulation of the mechanical behaviour of rayon mono-ply twisted yarns, at the macroscopic level. A yarn was represented by an equivalent three-dimensional solid of cylindrical shape with helicoidal anisotropy. The constitutive law accounts for visco-elastic and visco-plastic dissipation mechanisms and includes the direction of the fibres in the free energy definition.

In [3] we extended the above approach to multi-ply yarns by making recourse to the definition of properly oriented virtual fibres within a cord equivalent continuum cylinder, endowed with local anisotropic properties. This is achieved by exploiting the following three ingredients: the idealised analytical description of filament trajectories proposed by Treloar [4]; an averaging process (better detailed further on in this paper) which leads to define axial symmetric inclinations (with respect to cord axis) of virtual fibres considered present in the continuum cylinder; the experimental measurement of the cord cross section. In [2] this approach was implemented and numerically tested only with reference to 2-ply cords.

Cords made up of three yarns are often used as rubber reinforcements and in the literature several papers can be found describing experimental results on 3-ply cords of different polymeric materials, see e.g. [5, 6]. On the contrary very few contributions exist on the modelling of 3-ply cords, at the macroscopic scale, but accounting for the cord inner structure (e.g. the cord/yarn twist levels). The present contribution goes in the direction just mentioned by extending what already developed in [3] to treat the case of 3-ply cords. Another very interesting research line on the modelling of cords is reported in [7, 8] where the problem is tackled in large strain regime and a cord twisting simulation is incorporated in the analysis procedure.

In the present work, numerical simulations of 3-ply rayon cords are compared with experimental data on greige and dipped specimens under uniaxial tests conducted at different strain rates at Indorama Ventures Mobility Cremona SpA. Bending tests of dipped cords, conducted at Pirelli Laboratories (Milan), are also simulated.

2 ELASTO-VISCO-PLASTIC CONSTITUTIVE MODEL

The multi-ply yarns are modelled as anisotropic solids endowed with a constitutive law accounting for visco-elastic and visco-plastic dissipation mechanisms. The directions of anisotropy are defined by a local vector $\boldsymbol{a}$ related to the filament inclination inside the cord (see fig. 1). The constitutive model was formulated by the Authors in [2] and is described by the following governing equations, which can be subdivided into

• State equations

$$\boldsymbol{\sigma} = \boldsymbol{C} : (\boldsymbol{\varepsilon} - \boldsymbol{\varepsilon}^{ve} - \boldsymbol{\varepsilon}^{vp}) \qquad \text{Hooke's law} \tag{1}$$

$$\chi = h\,\gamma \qquad \text{Isotropic hardening rule} \tag{2}$$

$$\boldsymbol{X}_\ell = H_\ell\,\boldsymbol{\alpha}_\ell \qquad \text{Linear kinematic hardening rule} \tag{3}$$

$$\boldsymbol{X}_{n\ell} = H_{n\ell}\,\boldsymbol{\alpha}_{n\ell} \qquad \text{Nonlinear kinematic hardening rule} \tag{4}$$

• Evolution equations

$$\dot{\boldsymbol{\varepsilon}}^{ve} = \boldsymbol{\Xi}^{-1} : (\boldsymbol{\sigma} - \tilde{\boldsymbol{C}} : \boldsymbol{\varepsilon}^{ve}) \qquad \text{Viscoelastic strain} \tag{5}$$

$$\dot{\boldsymbol{\varepsilon}}^{vp} = \frac{\langle \varphi \rangle}{\eta}\,\text{sign}((\boldsymbol{\sigma} - \boldsymbol{X}_\ell - \boldsymbol{X}_{n\ell}) : (\boldsymbol{a} \otimes \boldsymbol{a}))(\boldsymbol{a} \otimes \boldsymbol{a}) \qquad \text{Viscoplastic strain} \tag{6}$$

$$\dot{\gamma} = \frac{\langle \varphi \rangle}{\eta} \qquad \text{Internal variable of isotropic hardening} \tag{7}$$

$$\dot{\boldsymbol{\alpha}}_\ell = \dot{\boldsymbol{\varepsilon}}^{vp} \qquad \text{Internal variable of linear kinematic hardening} \tag{8}$$

$$\dot{\boldsymbol{\alpha}}_{n\ell} = \dot{\boldsymbol{\varepsilon}}^{vp} - \frac{\langle \varphi \rangle}{\eta}\,\frac{B}{H_{n\ell}}\boldsymbol{X}_{n\ell} \qquad \text{Internal variable of nonlinear kinematic hardening} \tag{9}$$

• Yield condition

$$\varphi = |(\boldsymbol{\sigma} - \boldsymbol{X}_\ell - \boldsymbol{X}_{n\ell}) : (\boldsymbol{a} \otimes \boldsymbol{a})| - \sigma_y - \chi\ . \tag{10}$$

In the above relations, $\boldsymbol{\sigma}$, χ, $\boldsymbol{X}_\ell$, $\boldsymbol{X}_{n\ell}$ denote the stress and the static internal hardening variables; $\boldsymbol{\varepsilon}$, $\boldsymbol{\varepsilon}^{ve}$ and $\boldsymbol{\varepsilon}^{vp}$ denote the total, viscoelastic and viscoplastic strains; γ, $\boldsymbol{\alpha}_\ell$, $\boldsymbol{\alpha}_{n\ell}$ are

the kinematic internal variables describing isotropic, linear and nonlinear kinematic hardening; the scalars h, H_ℓ, $H_{n\ell}$, η, B and σ_y are material defined parameters.

In eq. (1) $\boldsymbol{C}$ is a fourth-order tensor representing the elastic stiffness of the material and its expression in a global reference system can be found in [2].

Here the transversely isotropic elastic law is expressed for simplicity in a local reference system where the z-axis coincides with the reinforcement direction $\boldsymbol{a}$, and, using matrix notation, it reads

$$\begin{bmatrix} \sigma_{xx} \\ \sigma_{yy} \\ \sigma_{zz} \\ \sigma_{xy} \\ \sigma_{xz} \\ \sigma_{yz} \end{bmatrix} = \begin{bmatrix} \frac{1-\nu_{PL}\nu_{LP}}{E_P E_L \Delta} & \frac{\nu_P+\nu_{LP}\nu_{PL}}{E_P E_L \Delta} & \frac{\nu_{LP}+\nu_P\nu_{LP}}{E_P E_L \Delta} & 0 & 0 & 0 \\ \frac{\nu_P+\nu_{PL}\nu_{LP}}{E_L E_P \Delta} & \frac{1-\nu_{LP}\nu_{PL}}{E_L E_P \Delta} & \frac{\nu_{LP}+\nu_{LP}\nu_P}{E_L E_P \Delta} & 0 & 0 & 0 \\ \frac{\nu_{PL}+\nu_P\nu_{PL}}{E_P^2 \Delta} & \frac{\nu_{PL}+\nu_{PL}\nu_P}{E_P^2 \Delta} & \frac{1-\nu_P^2}{E_P^2 \Delta} & 0 & 0 & 0 \\ 0 & 0 & 0 & \frac{E_P}{2(1+\nu_P)} & 0 & 0 \\ 0 & 0 & 0 & 0 & \mu_{LP} & 0 \\ 0 & 0 & 0 & 0 & 0 & \mu_{LP} \end{bmatrix} \begin{bmatrix} \varepsilon_{xx} \\ \varepsilon_{yy} \\ \varepsilon_{zz} \\ 2\varepsilon_{xy} \\ 2\varepsilon_{xz} \\ 2\varepsilon_{yz} \end{bmatrix} \tag{11}$$

where the subscript L denotes the longitudinal direction (assumed aligned with z), the index P denotes the transverse plane of isotropy (x-y); E_L and E_P are the elastic moduli, μ_{LP} is the shear modulus and ν_{PL}, ν_{LP} and ν_P are Poisson's coefficients; the term Δ is defined as

$$\Delta = \frac{(1+\nu_P)(1-\nu_P-2\nu_{PL}\nu_{LP})}{E_P^2 E_L}. \tag{12}$$

The following condition is assumed to hold to ensure the symmetry of the stiffness matrix

$$\frac{\nu_{PL}}{E_P} = \frac{\nu_{LP}}{E_L} \ . \tag{13}$$

The positive definiteness of the stiffness matrix is ensured when the following relations hold

$$E_P > 0, \quad E_L > 0, \quad \mu_{LP} > 0 \tag{14}$$

$$|\nu_P| < 1 \tag{15}$$

$$|\nu_{LP}| < \sqrt{\frac{E_L}{E_P}} \tag{16}$$

$$1 - \nu_P^2 - 2\nu_{LP}\nu_{PL} - 2\nu_P\nu_{LP}\nu_{PL} > 0 \ . \tag{17}$$

The viscoelastic stiffness tensor $\tilde{\boldsymbol{C}}$ has a form similar to the tensor $\boldsymbol{C}$ and is taken to be proportional to the elastic stiffness, resulting in $\tilde{\boldsymbol{C}} = \tilde{c}\boldsymbol{C}$. Similarly, the fourth-order tensor describing the retardation times is simplified to $\boldsymbol{\Xi} = \tilde{\theta}\tilde{\boldsymbol{C}}$, assuming a single retardation time $\tilde{\theta}$.

When under compression, the fibres are prone to instability, significantly reducing their effective stiffness. To address this behaviour in the constitutive model, we use a "piecewise" linear formulation as proposed in [9]. To this purpose, it is necessary to define when a material point is in a "state of tension" or a "state of compression" while preserving material symmetries in both states. To enforce a piecewise differentiable stress-strain law, the interface between tension

and compression states must be defined as a linear combination of the elastic strain in terms of invariants, as detailed in [9]. In this work, we assume that the interface is defined by a null value of the projection along the fibres of the elastic strain, namely

$$\boldsymbol{\varepsilon}^e : (\boldsymbol{a} \otimes \boldsymbol{a}) = 0 \ . \tag{18}$$

By exploiting the continuity of the stress function, the only engineering parameter that can jump across the interface is hence the longitudinal modulus E_L. For greige rayon, the ratio of longitudinal modulus for tension and compression is taken approximately equal to the value adopted in [10]

$$E_{L+} = 300 E_{L-} \ . \tag{19}$$

3 DOUBLY-WOUND HELIX MODEL OF 3-PLY CORDS

The mechanical response of twisted multi-ply yarns is directly influenced by the local orientation of the fibres, namely the angle that each filament makes with the cord axis. In principle, this angle can be obtained from microtomography measurements, as done in [1].

Since such refined experimental measurements are not available for the 3-ply cord here considered, we rely on the theoretical approach proposed in [4] by Treloar for cords made up of "doubly-wound" filaments, with the central fibre of each yarn following a helical trajectory. Although this model is usually employed for 2-ply cords [4, 11, 3], it can also be used for 3-ply cords (see fig. 1).

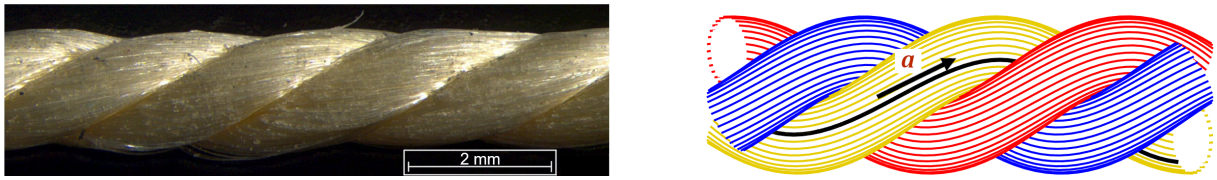

(a) (b)

Figure 1: (a) Microscopy of 3-ply cord, (b) schematic view of the fibres of the three yarns in blue, red and yellow; and definition of the unit vector $\boldsymbol{a}$ tangent to the fibre highlighted in black.

In the latter case, the idealised geometry of the cord depends on four parameters: n, number of filament twists per unit length; N, number of yarn twists per unit length; R_y, yarn radius; and the distance b between yarn axis and cord axis. The parameter n only influences the filament paths inside each yarn, while the remaining three define the outer geometry of the cord, represented in fig. 2 (a)-(c). For the case when $N = 380$ twists per metre (tpm) and $R_y = 0.23$ mm, it turns out that by choosing $b = 0.29$ mm, the idealised horizontal sections of the three yarns become exactly tangent to each other as in fig. 2 (c) (thus ensuring no material interpenetration). The horizontal cross-section of a real 3-ply rayon cord is depicted in fig. 2 (d); its three-lobed shape differs significantly from the theoretical section of fig. 2 (c) which presents an unrealistic hole at the centre. We assume that the actual cord cross-section is circular, with an area $A_{exp} = 0.55$ mm^2 (estimated using microscopy image).

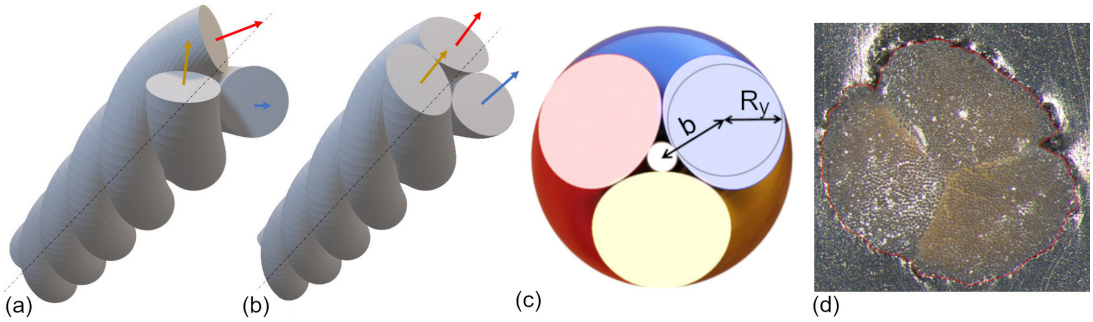

Figure 2: 3-ply cord: (a) perspective view of the cord with right cross sections of the three yarns, (b) perspective view of the cord with its right cross-section (c) cross sections of the three yarns in a plane perpendicular to the cord axis (d) microscopy of the cross-section of the cord inside rubber showing a three-lobes shape.

The Treloar's theory gives an analytical formula for the angle ϑ formed by the filaments with the cord axis. The contour plot of such angle is shown in fig. 3 (a). At this point, we follow the same logical steps already used in [3]: we compute the mean value of ϑ over a pitch length of the cord by considering that the cross section of the 3 yarns represented in fig. 3 (a) rotates when the section is taken in different positions along the cord axis. This mean value, which turns out to be axially symmetric, is denoted as $\vartheta = \vartheta(r)$, where $(b - R_y) \leq r \leq (b + R_y)$. This function is the red (upper) curve plotted in fig. 3 (b).

However, similarly to the case of 2-ply cords, we need to transform the relation $\vartheta = \vartheta(r)$ into a new one, $\vartheta^* = \vartheta^*(r^*)$, with $0 < r^* < R_{exp}$, where R_{exp} is the radius of the experimentally determined cross-section area A_{exp} of the cord.

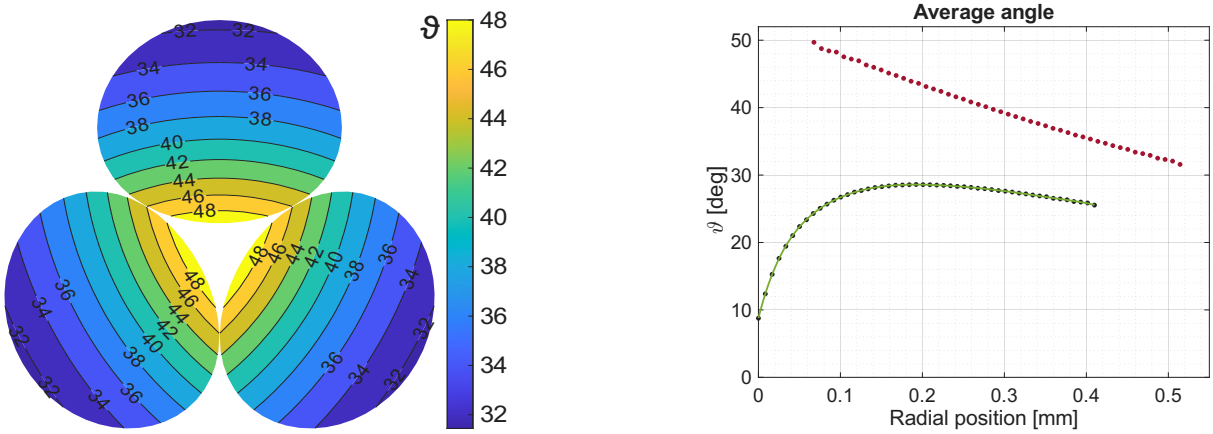

(a) (b)

Figure 3: (a) Fibre inclination on cross sections of the three yarns in a plane perpendicular to the cord axis; (b) mean fibre inclination versus radial position on the cross-section of the hollow cylinder enveloping the three yarns (in red) and, after transformation, on the cross-section of the equivalent cylinder representing the 3-ply cord (in green).

The adopted function $\vartheta^* = \vartheta^*(r^*)$ is the green (lower) curve, plotted in fig. 3 (b), and has been obtained by a rescaling of $\vartheta = \vartheta(r)$ analogous to the one described in [3] (preserving the fibre length), followed by a translation which eliminates the central hole. Such angle distribution $\vartheta^* = \vartheta^*(r^*)$ agrees, at least qualitatively, with the experimentally determined angle distribution reported in [1] in the case of a 3-ply cord made of nylon filaments.

Once the directions of the virtual fibres in the cord-equivalent continuum cylinder are defined, the analysis procedure requires the discretisation of the cylinder into FEs and the enforcement of the anisotropic constitutive law at the element Gauss points, where the fibre direction unit vector $\boldsymbol{a}$ must have been preliminarily calculated. All the numerical results described in the next Section have been obtained by using 20-node quadratic hexahedral elements, with reduced integration (8 Gauss points per element).

4 RESULTS OF SIMULATIONS AND COMPARISON WITH EXPERIMENTS

Table 1 gives the constitutive parameters here adopted for the analysis of greige 3-ply rayon cords, also indicated by symbol C3. The parameters are identical to those used in [3] for the simulation of reinforcements of the same rayon material but with different internal structure. More precisely, we recall that such a parameter set was determined based on tensile tests on untwisted and twisted single-ply yarns. Since the numerical results on 3-ply cords that we are going to describe in the next subsections show a good agreement with corresponding experimental data, we can claim that the present study represents further a validation of the overall analysis approach developed in [2, 3] and carried over to 3-ply cords in the present contribution.

Table 1: Material model parameters for rayon in humid conditions.

E_P [MPa]	E_{L+} [MPa]	E_{L-} [MPa]	ν_P [-]	ν_{LP} [-]	μ_L [MPa]	$\tilde{c}$ [-]
170	14500	48.3	0	0	10	4.00
$\tilde{\theta}$ [s]	σ_y [MPa]	H_ℓ [MPa]	$H_{n\ell}$ [MPa]	h [MPa]	B [-]	η [s MPa]
2.50	60	2700	40000	1200	1000	2000

4.1 Uniaxial tensile tests of greige 3-ply cords

The simulations of the tensile tests on greige cords C3 are carried out using the finite element discretisation which, on the cross-section, is visualised in fig. 5. The numerical global force-strain curves obtained with this mesh are compared to the corresponding experimental ones, for various strain rates, in fig. 4.

It can be noted that there is a good agreement up to a cord strain value of about $\varepsilon = 0.1$. In fig. 4 (b) both the longitudinal normal stress σ_3 and the normal stress along the (local) fibre direction σ_{fibre} are plotted along the radius, for $\varepsilon = 0.1$ and an adopted strain rate $\dot{\varepsilon} = 0.003$ s^{-1}. One can observe a non-monotonic variation of these stresses along the radius which reflects the peculiar distribution of the equivalent fibre inclination shown in fig. 3 (b) which is non-monotonic as well.

Contour plots of the normal stresses in the direction 3 of the cord axis and of the corresponding plastic strains are represented in fig. 5 for $\varepsilon = 0.1$. As expected, the zones with higher plastic

strain (i.e. the centre and the external layer) are those where fibres are less inclined (smaller ϑ): such fibres are more stressed and are the first to enter the plastic regime.

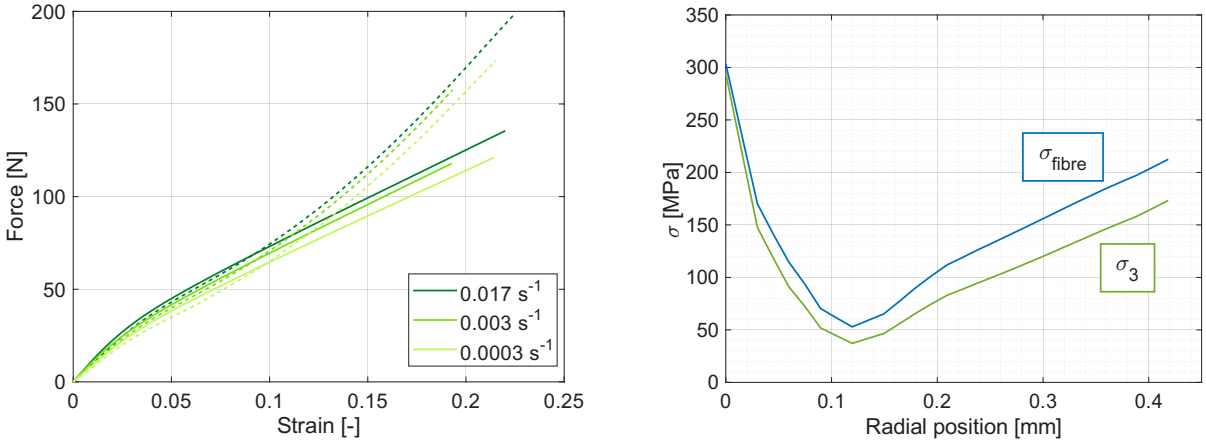

(a) (b)

Figure 4: (a) Uniaxial tensile test on cords C3 at different strain rates, experimental (dashed lines) and numerical (continuous lines); (b) axial stress versus radial position for $\varepsilon = 0.1$ and $\dot{\varepsilon} = 0.003$ s^{-1}.

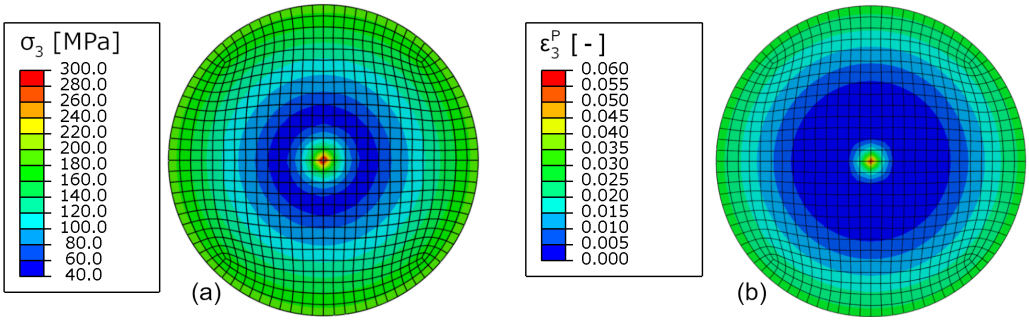

Figure 5: Contour plots of (a) normal stress and (b) longitudinal plastic strain in the direction of the cord axis, in cord C3 at a total cord strain of $\varepsilon = 0.1$.

4.2 Bending and uniaxial tensile tests of dipped 3-ply cords

When dealing with dipped cords, also denoted by symbol DC3, the presence of the adhesive in the outer layer must be taken into account. The thickness of such layer is assumed to be 36 μm. When meshing the equivalent cylinder representing the cord, we choose to adopt two quadratic finite elements in the radial direction to discretise the outer portion of the cord where the adhesive is present. In this zone, some of the elastic parameters are changed to account for the stiffening effect of the adhesive with respect to the values reported in table 1 for greige cords. Specifically E_P, E_{L-}, ν_P and μ_{LP} are increased.

Since the effect of dipping is more evident for cords subject to bending, recourse is made to three-point bending tests on a cord fabric specimen containing 10 dipped 3-ply cords, to

calibrate the new material parameters using the experimental data coming from both the bending tests and the tensile tests (the latter on single cords DC3). The bending test is performed in accordance with ASTM D885. As shown in fig. 6 (a) the cord fabric sample initially rests across a 25 mm span opening, in a straight configuration. The specimen is supported by two short cylindrical bars (5 mm in diameter) forming the two "T's" visible in fig. 6 (a). The specimen is deflected by a depressor element (a cylindrical bar 6 mm in diameter) acting at the centre of the span, and the force required to move the depressor is recorded.

The simulation of the bending test is carried out using the FE model of fig. 6 (b) in which only a single DC3 cord is considered. A contact analysis is performed to ensure an accurate representation of the interactions between the deformable cord, the two support elements and the central depressor element, these three elements being represented as discrete rigid surfaces. Frictionless contact is considered. The analysis is performed in a geometrically linear setting (small strain and displacement) and therefore only the first stage of the bending test is simulated, for a vertical translation of the depressor element less than, say, 2.5 mm. The deformed shape of the cord model is shown in fig. 6 (c), just for half of the cord (due to symmetry).

Comparing numerical and experimental results relevant to cord DC3 for both uniaxial and bending tests (the latter in their initial phase), it turns out that a good fit is obtained in both cases by adopting the following set of parameter values for the cord zone affected by the presence of the adhesive: $E_P = 8000$ MPa, $E_{L-} = 290$ MPa, $\nu_P = 0.3$ and $\mu_{LP} = 90$ MPa. Since the bimodulus ratio E_{L-}/E_{L+} plays a greater role in bending, the calibration of E_{L-} stems substantially from the bending tests.

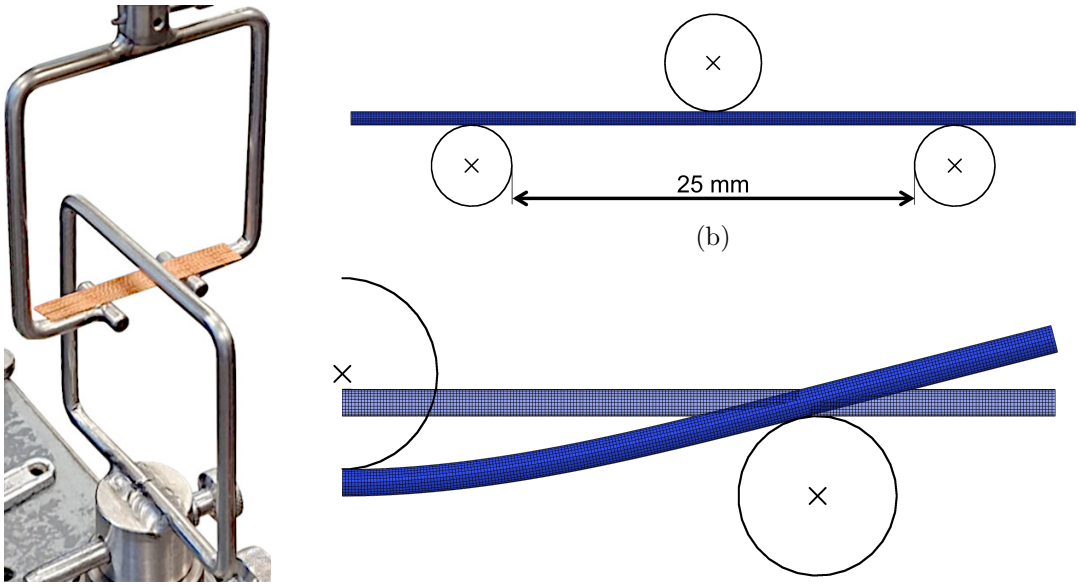

Figure 6: (a) Bending test on a cord fabric specimen containing 10 DC3 cords, based on ASTM D885; (b) FE model for simulating the bending of a single DC3 cord, in contact with rigid elements; (c) side view of half of the DC3 cord, in initial and deformed configuration (with maximum vertical displacement = 2.5 mm).

This set of parameters for the dipped outer layer of the cord and that of table 1 for the cord interior (without the adhesive) are used for the bending simulation. The mesh on the cross-section is represented in fig. 7 (a) where the smaller elements used for the outer dipped region are visible. The length of the finite elements in the longitudinal direction is such that the elements in the zone around the cord axis have an aspect ratio close to 1. The computed force versus mid-span displacement curve is represented in fig. 7 (b) (solid line) together with the corresponding experimental curve (dashed line). A very good agreement is obtained at least for values of the imposed mid-span displacement lower than 2.5 mm.

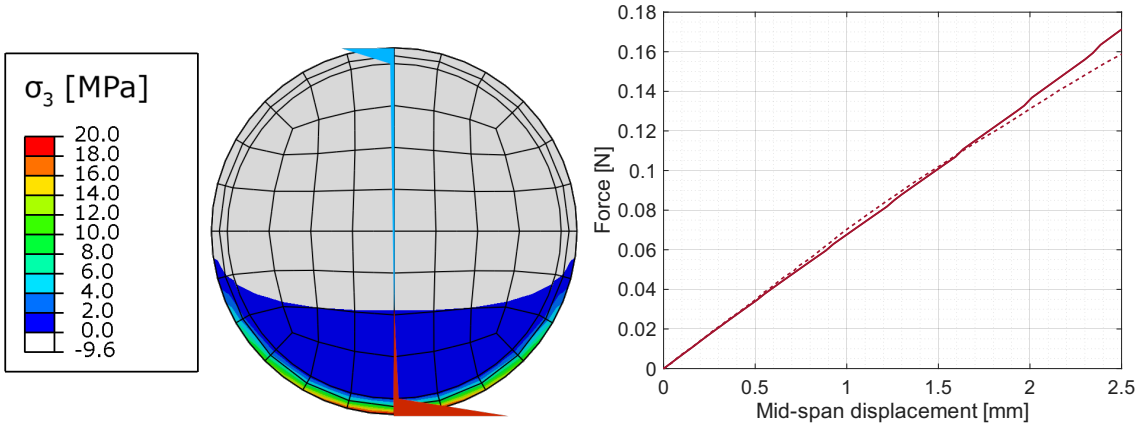

(a) (b)

Figure 7: (a) Stress distribution in the central (mid-span) section of the DC3 cord under bending load, which accounts for different behaviour in tension and compression; (b) initial portion of the force-displacement curve for the 3-point bending test of the cord fabric (10 cords of type DC3): experimental curve (dashed line) and numerical result from FE model (solid line).

Figure 7 (a) displays the contours of normal stress σ_3 in the lower portion of the central section of the cord, where the stress is positive. The region in light-grey is subjected to $\sigma_3 < 0$. One can observe that, due the inclusion of the bimodular effect, the neutral axis is below the centre and the stress distribution along the vertical diameter is not symmetric (tension is represented in red and compression in light-blue).

As for the simulations of the uniaxial tensile tests whose results are shown in fig. 8, the adopted finite element mesh is the one of fig. 5. Figure 8 (a) shows experimental and numerical results for the uniaxial tests of cords DC3, at different strain rates. A good agreement is obtained at least for strains up to $\varepsilon = 0.08$. Figure 8 (b) shows that, with the adopted set of parameters previously specified, it is possible to have a good agreement between experimental and numerical response for both the greige cord C3 and the dipped cord DC3.

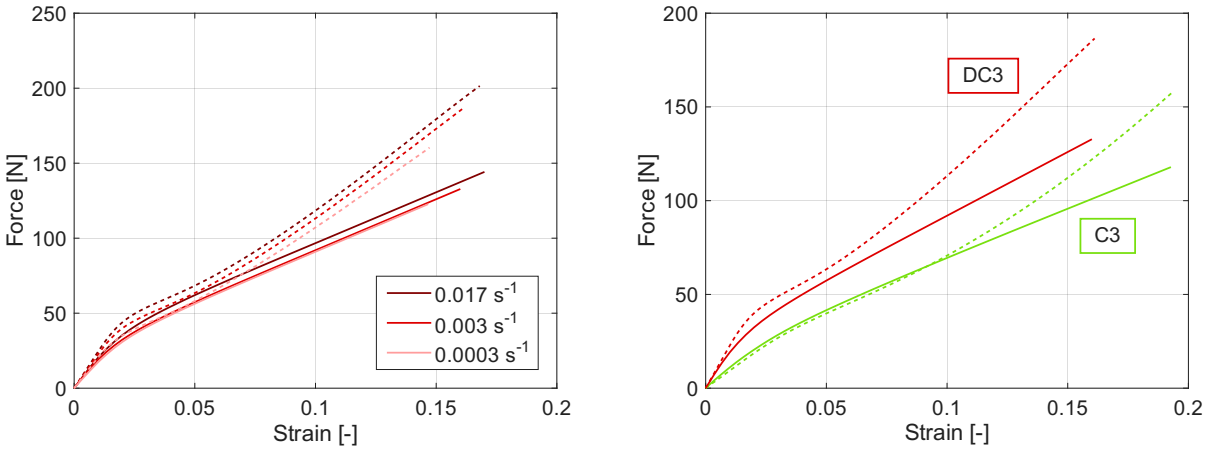

(a) (b)

Figure 8: (a) Uniaxial tensile test of dipped cords DC3 at different strain rates ($\dot{\varepsilon}$ = 0.017 s^{-1}, 0.003 s^{-1}, 0.0003 s^{-1}), experimental data (dashed lines) and numerical results (solid lines); (b) uniaxial tensile test on greige and dipped cords, C3 and DC3, at a strain rate of 0.003 s^{-1}: experimental data (dashed lines) and numerical results (solid lines).

5 CONCLUSIONS

In the present study the computational procedure for simulating the behaviour of multi-ply yarns which was developed in [3] has been extended to 3-ply cords. The model shows a very good quantitative agreement with experimental force-strain responses for cord tensile strains up to 10%.

By incorporating a bimodular effect, the model captures the different response of the fibres under tension and compression, which is particularly important for analysing the cord response under bending. For dipped cords, by adjusting the material parameters for the outer layer, where the adhesive is present, a good fit can be obtained with experimental data for both tensile and bending tests.

Moreover, the model allows the estimation of local stress and strain distributions, which are influenced by fibre inclination and cord construction. This capability paves the way for optimizing cord designs. Future work will focus on extending the model to include large displacements and the possible reorientation of the fibres, thereby broadening the applications range of the proposed approach.

REFERENCES

[1] A. Sibellas, J. Adrien, D. Durville, and E. Maire, "Experimental study of the fiber orientations in single and multi-ply continuous filament yarns," *Journal of the Textile Institute*, vol. 111, pp. 646–659, 5 2019.

[2] M. Moscatelli, L. Pires da Costa, P. Caracino, S. Agresti, G. Novati, and C. Comi, "Elasto-viscoplastic model for rayon yarns," *Meccanica*, vol. 59, pp. 793–810, 5 2024.

[3] L. Pires da Costa, M. Moscatelli, P. Caracino, G. Novati, and C. Comi, "Geometrical and mechanical modeling of polymeric multi-ply yarns," *Applied Sciences (Switzerland)*, vol. 14, pp. 1–13, 6 2024.

[4] L. Treloar, "The geometry of multi-ply yarns," *Journal of the Textile Institute Transactions*, vol. 47, pp. T348–T368, 6 1956.

[5] P. R. Willett, "Viscoelastic properties of tire cords," *Journal of Applied Polymer Science*, vol. 19, pp. 2005–2014, 1975.

[6] B. Chen, "Material characterization of tire cords and the effects of cord thermal-mechanical properties on tires," *Tire Science and Technology, TSTCA*, vol. 32, no. 1, pp. 2–22, 2004.

[7] H. Donner, *FEM-basierte Modellierung stark anisotroper Hybridcord-Elastomer-Verbunde*. PhD thesis, Technischen Universität Chemnitz, 2017.

[8] S. Weiser, T. Lehmann, R. Landgraf, N. Goldberg, H. Donner, and J. Ihlemann, "Experimental and numerical analysis of cord–elastomer composites," *Journal of Rubber Research*, vol. 24, pp. 211–225, 6 2021.

[9] A. Curnier, Q.-C. He, and P. Zysset, "Conewise linear elastic materials," *Journal of Elasticity*, vol. 37, pp. 1–38, 1995.

[10] C. W. Bert, "Models for fibrous composites with different properties in tension and compression," *Journal of Engineering Materials and Technology*, vol. 99, no. 4, pp. 344–349, 1977.

[11] B. S. Jeon and Y. J. Kim, "Orientation density function of ply yarn," *Textile Research Journal*, vol. 80, no. 15, pp. 1550–1556, 2010.